Suppression of twinning and phase transformation in an ultrafine grained 2 GPa strong metastable austenitic steel: Experiment and simulation

Y.F. Shen [a], N. Jia [a,*], Y.D. Wang [a], X. Sun [b], L. Zuo [a], D. Raabe [c,*]

[a] Key Laboratory for Anisotropy and Texture of Materials (MOE), Northeastern University, Shenyang 110004, P.R. China
[b] Computational Science and Mathematics Division, Pacific Northwest National Laboratory, Richland, WA 99352, USA
[c] Max-Planck-Institut für Eisenforschung, D-40237 Düsseldorf, Germany

ABSTRACT

An ultrafine-grained 304 austenitic 18 wt.% Cr–8 wt.% Ni stainless steel with a grain size of ∼270 nm was synthesized by accumulative rolling (67% total reduction) and annealing (550 °C, 150 s). Uniaxial tensile testing at room temperature reveals an extremely high yield strength of 1890 ± 50 MPa and a tensile strength of 2050 ± 30 MPa, while the elongation reaches 6 ± 1%. Experimental characterization on samples with different grain sizes between 270 nm and 35 μm indicates that both, deformation twinning and martensitic phase transformation are significantly retarded with increasing grain refinement. A crystal plasticity finite element model incorporating a constitutive law reflecting the grain size-controlled dislocation slip and deformation twinning captures the micromechanical behavior of the steels with different grain sizes. Comparison of simulation and experiment shows that the deformation of ultrafine-grained 304 steels is dominated by the slip of partial dislocations, whereas for coarse-grained steels dislocation slip, twinning and martensite formation jointly contribute to the shape change.

© 2015 Acta Materialia Inc. Published by Elsevier Ltd. All rights reserved.

1. Introduction

Non-alloyed metallic materials can be equipped with ultrahigh strength by employing heavy plastic deformation and/or by creating ultrafine-grained (UFG) microstructures. Here UFG materials are defined as polycrystalline solids with property-controlling grain structures below the scale of 1 μm. Typical processing routes include severe plastic deformation (SPD) [1,2], which decomposes grains through dislocation accumulation and reorganization (polygonization). Several different SPD processes for manufacturing bulk materials typically include equal-channel angular pressing (ECAP) [3], high-pressure torsion (HPT) [4] and accumulative roll-bonding (ARB) [5]. In case of steels, UFG structures can also be obtained via thermomechanical processing, exploiting the interplay between plastic deformation, recrystallization and phase transformation [6–11]. One of the main motivations for obtaining very fine grains is motivated by the increase in mechanical strength according to the Hall–Petch relationship [12]. However, such enabled UFG structured ultra-high strength metals often loose ductility compared to their conventional coarse-grained

(CG) counterparts. The drop in ductility of UFG metals is attributed to inhomogeneous deformation at microstructural level, leading to early plastic localization and the premature onset of damage [2]. For example, a nano-grained (NG) 316L austenitic stainless steel (with an average grain size of 40 nm) prepared via surface mechanical attrition treatments exhibits an extremely high yield strength of 1450 MPa, whereas the ductility is limited to a few percent [2]. Interesting strategies have been proposed for simultaneously increasing the ductility and strength of UFG pure copper and nanostructured alloys [13–17]. In pure copper, high ductility can be achieved without sacrificing strength by introducing a high density of pre-existing twins and a large fraction of high-angle grain boundaries. These encouraging results motivated the current study in an effort to obtain both, high strength and good ductility from a bulk alloy.

The 304 stainless steel (SS), a meta-stable austenite alloy, has been widely used in many industrial areas due to its excellent combination of strength and formability, high corrosion resistance and weldability. 304SS contains approximately 18 wt.% Cr and 8 wt.% Ni [18]. According to the carbon concentration, the 304SS can be divided into three groups, i.e. 304L SS with less than 0.03 wt.% carbon content, 304SS with 0.03–0.06 wt.% carbon, and 304H SS with a carbon content above 0.06 wt.%. The addition of

---

∗ Corresponding authors.
  E-mail addresses: jian@atm.neu.edu.cn (N. Jia), d.raabe@mpie.de (D. Raabe).

Cr enables corrosion resistance while Ni and C stabilize the austenitic phase and tune its thermodynamic stability. During room temperature torsion testing, 304L SS can withstand severe shear deformation (~2.55 true strain), resulting in a remarkable volume fraction of transformed bcc martensite of 63.5% [19]. However, synchrotron X-ray diffraction study on the phase transformation kinetics and texture evolution of a 304L SS steel subjected to conventional compression testing [20] revealed phase transformation only at cryogenic temperatures (−70 °C). An in-situ X-ray micro-diffraction study in conjunction with uniaxial tensile loading conducted at −63 °C substantiated the occurrence of a phase-transformation-enhanced strain/stress accommodation mechanism in this material [21].

Metastable variants of such austenitic SSs have attracted great interest because of their high strength and ductility when equipped with an ultrafine grain size. [22]. In wet air, even the resistance to corrosion of such UFG SS increases with decreasing grain size, which is attributed to the effect that the many abundant grain boundaries facilitate diffusion of Cr towards the surface during oxidation [23,24]. Heavy cold-rolling in conjunction with subsequent short-time annealing of 304SS is an efficient approach to refine the grain size. The basis for this processing is due to the effect that the initial heavy cold rolling of a metastable austenitic SS leads to very fine lath- and dislocation cell-type transformation martensite which then transforms into ultrafine austenite grains upon annealing [22]. In addition, it is reported that warm rolling and thermal cycling [25] can lead to significant grain refinement in a 304SS based on the mechanisms of continuous dynamic recrystallization [26–31].

Several works have shown that twinning and martensitic transformation play key roles for the deformation of 304SS and that the volume fraction of martensite formed during severe deformation is strongly dependent on the pre-strain, stress and strain magnitude, strain rate, and deformation temperature [21,32–38]. In that context earlier papers reported nanoscale embryos of martensite within the microstructure of a tensile deformed austenitic steel [21,36]. These various observations and phenomena encouraged us to explore the feasibility of obtaining bulk UFG steels through severe plastic deformation, particularly via accumulative rolling. Therefore, in the present study, a series of austenitic stainless steels with different grain sizes (ranging from 270 nm to 35 μm) were prepared by means of accumulative rolling and annealing. Uniaxial tensile testing shows that the UFG steel with a grain size of 270 nm exhibits an extremely high yield strength of 1890 ± 50 MPa and a tensile strength as high as 2050 ± 30 MPa, while the elongation reaches 6 ± 1%. The conventionally synthesized reference sample with 35 μm grain size showed 220 MPa yield strength, 1640 MPa tensile strength and 59% elongation to fracture. To explore the micromechanical behavior of the UFG austenitic steels, transmission electron microscopy (TEM) observations of the deformed microstructure as well as crystal plasticity finite element (CPFE) modeling of the tensile deformation for the steels with various grain sizes are performed.

2. Experiments

2.1. Experimental method

The material used in this study is a commercial 304SS with chemical composition of (wt.%): Cr 18.37, Ni 8.51, Mn 1.68, Si 0.72, P 0.03, C 0.02, N 0.06, $S < 0.01$, balanced by Fe. The fully annealed sheets with an initial thickness of 6 mm were held for 600 s at 400 °C in an electrical furnace under air atmosphere, and immediately rolled in a single-pass to 17% thickness reduction. The rolling was performed at a roll speed of 300 mm s^{-1} by a twin

roller. The workability can be promoted by rolling at elevated temperatures at an expense of accumulated strains. This process was repeated until a total reduction of 67% was reached. The final dimensions of the steel sheets were $300 \times 100 \times 1.5$ mm^3. The sheets were air-cooled after rolling. Subsequently, a series of heat treatments were further conducted to obtain samples with various grain sizes. The annealing temperatures varied from 550 °C to 950 °C with an increment of 100 °C. The holding time was 150 s for the sample annealed at 550 °C and the other samples were held for 180 s at the designed temperatures, respectively.

The as-prepared steel sheets were cut along the rolling direction (RD) into dog-bone shaped specimens, with a gauge length of 30 mm, width of 3 mm, and a final thickness of 1.5 mm after polishing. Uniaxial tensile tests were performed at an initial strain rate of 10^{-3} s^{-1} using a SANS micro-force testing system under room temperature. A contactless MTS LX300 laser extensometer was used to calibrate and measure the strain upon loading. Hardness measurements were performed with a MVD-401 Vickers hardness testing machine, with a load of 5 kg and a loading time of 10 s.

Cross sections were cut from the gauge of the deformed samples for evaluating the martensite volume fraction, using X-ray diffraction (XRD) analysis. Samples were chemically cleaned first using a mixture of HCl and HNO$_3$ in 2:1 ratio and then with C$_2$H$_5$OH to improve the precision of the analysis. The XRD measurement was performed on an X'Pert PRO diffractometer in conjunction with a Co anode operated at a $K\alpha$ wavelength of $\lambda = 0.1789$ nm. The penetration depth of this hard X-ray into the steel samples amounts to a few micrometers. The quantitative estimation of the α′-martensite phase content was based on the principle that the volume fraction of one constitutive phase is proportional to the integrated intensity of all diffraction peaks for that phase. Then the volume fraction of martensite can be calculated by measuring the integrated intensity of each reflecting plane of the phase from a single XRD scan. Details of the calculation method can be found in [23]. To reveal the crystallographic textures of the steels after annealing, the {1 1 1} and {2 2 0} pole figures of the annealed samples were measured by XRD using Co-$K\alpha$ radiation in reflection geometry.

The microstructure of the deformed specimens was studied by TEM. Specimens for TEM observation were cut from the deformed samples and mechanically polished to a thickness of about 60 μm. Subsequently the samples were polished with diamond paste, and then the foils were thinned using a double jet electrolytic polisher at a voltage of 32 V and a temperature between −10 and −5 °C. TEM observations of the samples were performed in a Tecnai G^2 20 microscope operated at an accelerated voltage of 200 kV.

2.2. Microstructure characterizations

Fig. 1(a) shows the X-ray diffraction patterns of the 304SS samples at different conditions. The calculated results indicate that the martensite (α′) decreases with increasing annealing temperature (Fig. 1(b)). For example, the martensite volume fraction is as high as 73% for the as-cold-rolled sample; however, it decreases to 10% after annealing at 850 °C for 180 s. The phenomenon indicates that the martensite induced by cold-rolling has been reversed to austenite (γ) during the annealing.

Our previous work, conducted using electron backscatter diffraction (EBSD) for characterizing the microstructures of the steels [39] has shown that for the samples annealed at 650 °C, 850 °C and 950 °C for 180 s, the average grain size increases from 800 nm to 10 μm and 35 μm with increasing annealing temperature. However, for the sample annealed at 550 °C for 150 s the grain size is too small to be discerned by EBSD. Therefore, in this work TEM observations are performed to measure the grain size.
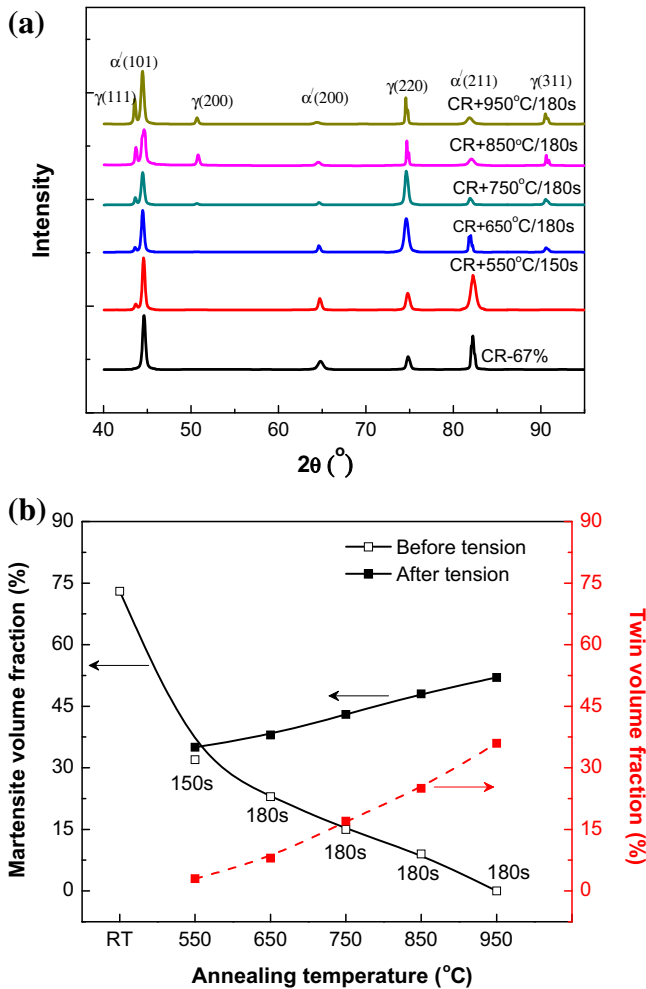
Fig. 1. (a) XRD patterns of the cold-rolled Fe–18.37Cr–8.51Ni–1.68Mn–0.72Si–0.02C–0.06N steel along with those annealed at different temperature and time. (b) The calculated volume fractions of martensite and deformation twin before and after tension, the annealing duration has been indicated for each data.

volume fractions of both martensite and deformation twinning increase as the annealing temperature is elevated (Fig. 1(b)). This surprising observation is attributed to the fact that a large amount of martensite and twins tend to be formed in the high temperature-annealed samples during the subsequent uniaxial tensile testing. The texture measurements reveal that after 550 °C annealing a minor Goss orientation ({110}⟨001⟩) with the maximum intensity of $f(g) \sim 3.9$ exists (Fig. 3). With increasing annealing temperature, this texture component weakens and the steel annealed at 950 °C shows a random crystallographic texture.

2.3. Mechanical properties determined by tensile tests

Fig. 4(a) shows the tensile true stress vs. strain curves for the 304 SS with various grain sizes at a strain rate of 10^{-3} s^{-1} at room temperature. In comparison with the reference coarse-grained steel (grain size ~35 μm), the UFG samples exhibit significantly higher strength. One can see that the tensile yield strength σ_y of the sample with 270 nm grain size (at 0.2% offset) is 1890 ± 50 MPa, i.e. about 8 times higher than that of the CG sample (~200 MPa), and the ultimate tensile strength (σ_{UTS}) is 2050 ± 30 MPa. The Vickers hardness of the sample is 5.6 GPa. This means that the strength of the sample is the same in tension and compression, i.e. the material is fully dense and free of porosity. For the sample with an average grain size of 800 nm, the values for σ_y and σ_{UTS} are 1170 ± 30 MPa and 1350 ± 40 MPa, respectively. The data show that both σ_y and σ_{UTS} increase with the refinement of grain size while the failure strain is reduced with decreasing grain size. The elongation-to-failure (ε_f) is 6 ± 1% (~0.06 true strain), 12 ± 2% (~0.12 true strain) and 59 ± 2% (~0.46 true strain) for the samples with a grain size of 270 nm, 800 nm and 35 μm, respectively. The reduced plasticity of the UFG samples is attributed to the reduced dislocation activity as will be discussed in Section 4.

3. Simulation of uniaxial tensile deformation

3.1. Constitutive formulations

3.1.1. Flow rule

We use the finite strain kinematic framework in which the deformation gradient, **F**, is multiplicatively decomposed according to:

$$\mathbf{F} = \mathbf{F}^e \mathbf{F}^p \tag{1}$$

where $\mathbf{F}^e$ is the elastic part comprising the stretch, $\mathbf{U}^e$, and the lattice rotation, $\mathbf{R}^e$; $\mathbf{F}^p$ is the plastic part of the deformation gradient. The initial plastic deformation gradient $\mathbf{F}_0^p$ is set to the inverse of the local crystal orientation, T_0^{-1}, and evolves at a rate governed by the plastic velocity gradient $\mathbf{L}^p$:

$$\dot{\mathbf{F}}^p = \mathbf{L}^p \mathbf{F}^p \tag{2}$$

The evolution of the crystal orientation with strain then follows from the polar decomposition $\mathbf{F}^e = \mathbf{R}^e \mathbf{U}^e$ as $T = \mathbf{R}^e$. As suggested by Kalidindi [40], the plastic velocity gradient, $\mathbf{L}^p$, contains shear contributions from dislocation slip systems (indexed by α) and twinning systems (indexed by β):

$$\mathbf{L}^p = \sum_{\alpha=1}^{12} \dot{\gamma}^\alpha \mathbf{m}^\alpha \otimes \mathbf{n}^\alpha + \sum_{\beta=1}^{12} \dot{\gamma}^\beta \mathbf{m}_{twin}^\beta \otimes \mathbf{n}_{twin}^\beta \tag{3}$$

The vectors **m** and **n** denote the normalized directions and plane normals of the deformation systems on which shear occurs at a rate of $\dot{\gamma}$. By omitting the volume fraction of the non-twinned crystal portions in the contribution of dislocation slip

Typical microstructures obtained at different areas of the sample are shown in Figs. 2(a)–(c). Many grains are equiaxed and the corresponding selected-area-electron-diffraction (SAED) pattern in Fig. 2(a) demonstrates that the mutual misorientation distribution among the grains is random with many high angle grain boundaries. The statistical result indicates that the average grain size of the sample is ~270 nm.

For the subsequently tensile deformed steels, as they exhibit quite different maximum elongations, the volume fraction of martensite and deformation twin obtained at various elongations for the samples after 550 °C, 650 °C and 950 °C annealing are listed in Table 1. At a strain of 6%, all steels show very low volume fractions of the martensitic phase transformation and twinning, indicating that dislocation slip is the main deformation mechanism. At 12% strain, the significant increase of martensite (~15 vol.%) as well as the occurrence of twins (~8 vol.%) is identified in the 650 °C annealed steel. However, in the 950 °C annealed steel, the increase of deformation twins (~13 vol.%) is more significant than that of the martensitic phase transformation (~5 vol.%). This suggests that with increasing straining mechanical twinning starts to play a large role in the high temperature-annealed steel. Still in this steel, when the maximum strain of 59% is reached, the martensite and twin volume fractions are 53% and 36%, respectively. Then it is obvious that at the ultimate strains for the studied steels, the
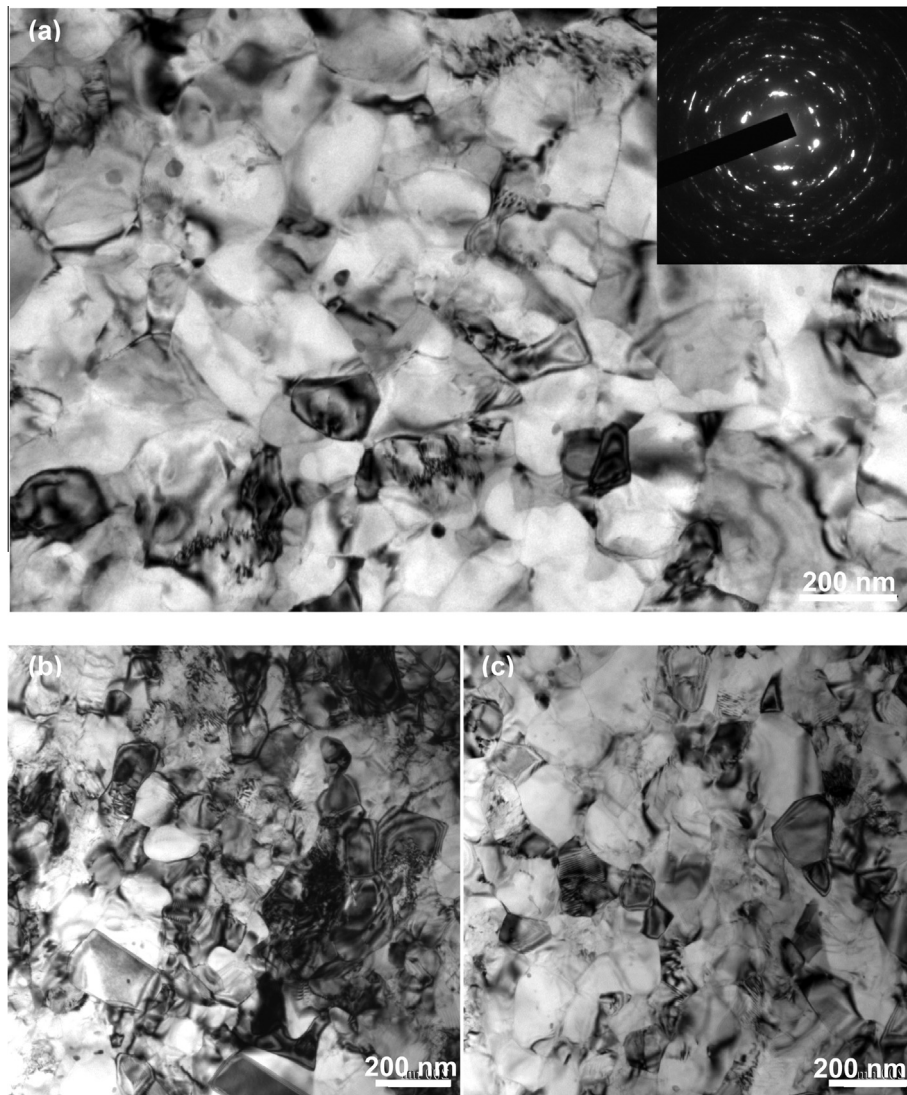
Fig. 2. Typical TEM micrographs showing the morphology of grains in the cold-rolled Fe–18.37Cr–8.51Ni–1.68Mn–0.72Si–0.02C–0.06N steel after annealing at 550 °C for 150 s. An inset in (a) shows the corresponding selected-area-electron-diffraction (SAED) pattern.

Table 1
Volume fractions of martensite and deformation twin in the steels at different elongations. The statistics for the martensite and twin are obtained from the XRD analyses and TEM observations, respectively.

Annealing temperature, average grain size	Volume fraction	0% elongation	6% elongation	12% elongation	59% elongation
550 °C, 270 nm	Martensite (%)	32	34	–	–
	Twin (%)	0	3	–	–
650 °C, 800 nm	Martensite (%)	23	26	38	–
	Twin (%)	0	5	8	–
950 °C, 35 μm	Martensite (%)	0	3	5	53
	Twin (%)	0	5	13	36

in Eq. (3) (in contrast to [40]), we (i) assume that twins can be sheared by dislocation slip in a compatible manner to the surrounding matrix, and (ii) ignore any potentially different evolution of slip resistance within them. For the austenitic phase, 12 $\{1\,1\,1\}\langle1\,1\,0\rangle$ dislocation slip systems and 12 $\{1\,1\,1\}\langle1\,1\,2\rangle$ twinning systems are considered. For the martensitic phase, two types of slip systems with a common $\langle1\,1\,1\rangle$ direction, i.e. $\{1\,1\,0\}\langle1\,1\,1\rangle$ and $\{1\,1\,2\}\langle1\,1\,1\rangle$, are considered, but no bcc twinning is included.

3.1.2. Dislocation slip

Conventional flow rules use a reference shear rate and a rate sensitivity exponent which are typically constant. Here, following Blum and Eisenlohr [41], the evolution of the dislocation densities is related to dislocation multiplication, dipole formation as well as dislocation annihilation. The flow rule describes thermally activated dislocation motion through forest dislocations. The shear rate of the slip system α is:
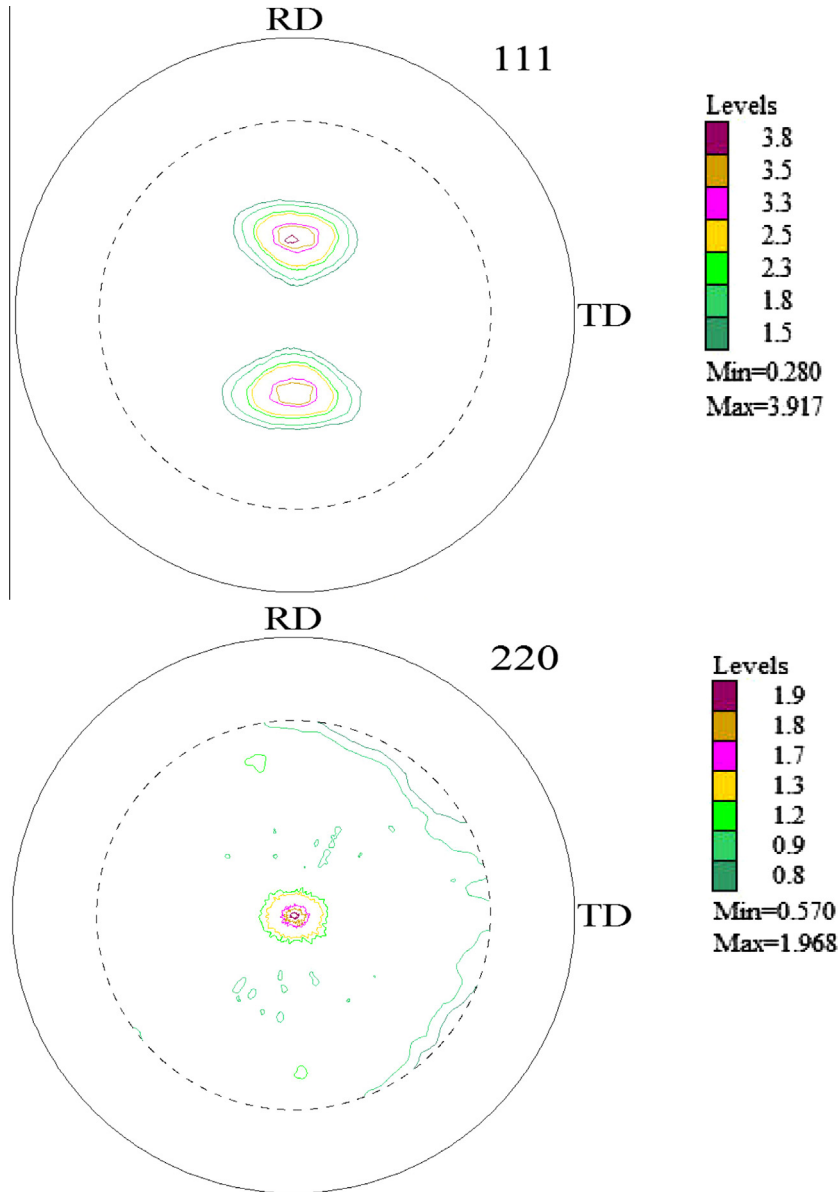
Fig. 3. {1 1 1} and {2 2 0} pole figures for the cold-rolled steel after annealing at 550 °C for 150 s.

$$\dot{\gamma}^{\alpha} = \rho_{\text{sgl}}^{\alpha} b v_0 \exp\left[\left(-\frac{Q_0}{k_B T}\left(1 - \frac{|\tau^{\alpha}|}{\hat{\tau}^{\alpha}}\right)^p\right)^q\right]\text{sign}(\tau^{\alpha}) \qquad (4)$$

where τ^{α} is the current resolved shear stress; $\hat{\tau}^{\alpha}$ is the slip resistance governed by the dislocation population; $\rho_{\text{sgl}}^{\alpha}$ is the unipolar dislocation density; b is the length of the Burgers vector; v_0 is the dislocation velocity of the slip system when subjected to a stress equal to the slip resistance $\hat{\tau}^{\alpha}$; Q_0 is the activation energy for dislocation slip; k_B and T denote the Boltzmann constant and temperature, respectively; p and q are numerical parameters to adjust the obstacle profile [42]. The slip resistance $\hat{\tau}^{\alpha}$ depends on the local dislocation densities as:

$$\hat{\tau}^{\alpha} = \tau_{\text{solute}} + Gb\left(\sum_{\alpha'=1}^{\text{Nslip}}\xi_{\alpha\alpha'}(\rho_{\text{sgl}}^{\alpha'} + \rho_{\text{dip}}^{\alpha'})\right)^{1/2} \qquad (5)$$

With τ_{solute} being a constant glide resistance stemming from solid solution effects, G the shear modulus, $\rho_{\text{dip}}^{\alpha'}$ the dipolar dislocation density, and $\xi_{\alpha\alpha'}$ characterizes the interaction strength among

different slip systems α and α'. For fcc metals, the possible interaction types include self, coplanar, collinear, orthogonal, glissile and sessile [43]. For bcc metals, only the self-interaction and the interaction between different slip systems are considered.

3.1.3. Mechanical twinning

The model accounts for the evolution of the twinned volume fraction. Following the twin nucleation model of Mahajan et al. [44], we assume that the critical twin nucleation event is the collective bow-out of three partial dislocations between pinning points that are separated by a critical length L_0. The associated critical stress for twin formation then reads

$$\hat{\tau}_{\text{twin}} = \frac{\gamma_{\text{sf}}}{3b_{\text{twin}}} + \frac{3Gb_{\text{twin}}}{L_0} \qquad (6)$$

where b_{twin} is the magnitude of the Burgers vector of the moving partials and γ_{sf} is the stacking fault energy. Using this critical stress formulation the mechanically driven twin nucleation rate is expressed as
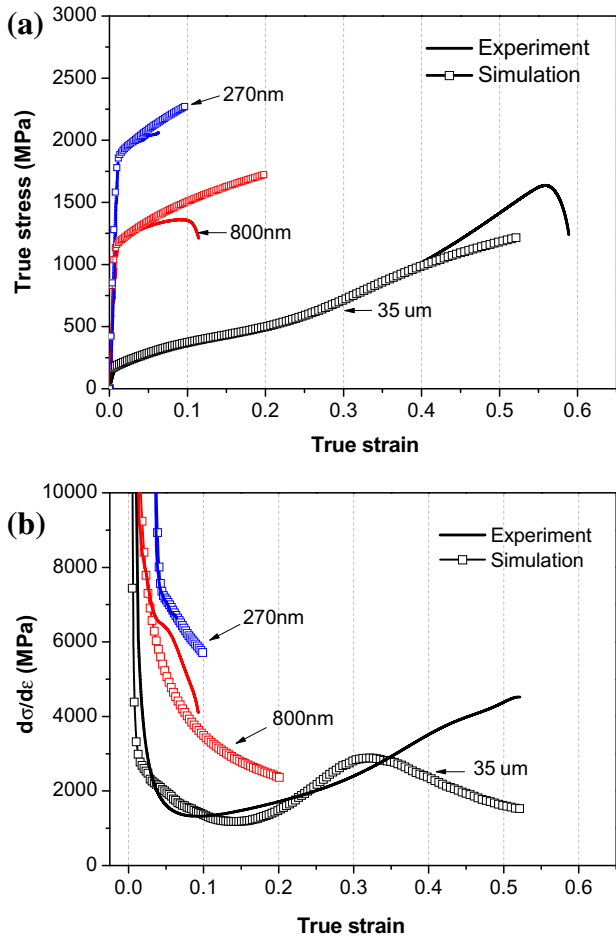
Fig. 4. (a) Measured and simulated true stress–strain curves for the steels with ultrafine grains (the average grain size is 800 nm and 270 nm, respectively) during uniaxial tensile tests, in comparison with the coarse-grained material (with an average grain size of 35 μm). Tensile loading is imposed parallel to the rolling direction of the as-prepared steel sheets. (b) Measured and simulated strain-hardening responses for the steels with different grain sizes.

$$\dot{N}^{\beta} = \dot{N}_0 \exp\left[-\left(\frac{\hat{\tau}_{\text{twin}}}{\tau^{\beta}}\right)^{r}\right] \qquad (7)$$

where τ^{β} is the resolved stress in the twin system, and $\dot{N}_0$ and r are fitting parameters. It is further assumed that the so formed twin expands instantaneously until encountering an obstacle, such as a grain or twin interface. The volume of the new deformation twin is

$$V^{\beta} = \frac{\pi}{6} s \lambda^{\beta 2} \qquad (8)$$

Here, s is a constant twin thickness, and λ^{β} is the effective distance between obstacles against twin growth,

$$\frac{1}{\lambda^{\beta}} = \frac{1}{d_{\text{grain}}} + \sum_{\beta'=1}^{12} \xi_{\beta\beta'} \frac{1}{d_{\text{twin}}^{\beta'}} \qquad (9)$$

d_{grain} is the constant grain size, and the twin spacing d_{twin} naturally evolves with the twin volume fraction as according to

$$d_{\text{twin}}^{\beta} = s(1-f)/f^{\beta} \qquad (10)$$

with f being the total volume fraction of the mechanical twins and f^{β} the volume fraction for the twin system β. The twin–twin interaction parameter $\xi_{\beta\beta'}$ is 0 for coplanar twin systems β and β' and 1 for non-coplanar systems. The resulting shear rate for each twin system is calculated as

$$\dot{\gamma}^{\beta} = (1-f)\gamma_{\text{twin}} V^{\beta} \dot{N}^{\beta} \qquad (11)$$

where γ_{twin} is the characteristic twin shear. Details of the dislocation and twinning models are described in [41,42]. For dislocation slip the rate equation of the dislocation density evolution is in the form $d\rho = \frac{|d\gamma^{\alpha}|}{b\lambda^{\alpha}}$, where λ^{α} is the effective (harmonic mean) distance between obstacles. With the presence of twins in the microstructure, the evaluation of λ^{α} then has to account for twin boundaries as additional obstacles against dislocation motion. The slip-twin interaction parameter $\xi_{\alpha\beta}$ is introduced for the slip system α and twin system β. If planes α and β are coplanar or β is a cross slip plane for α, $\xi_{\alpha\beta}$ assumes a value of 0. In all other cases $\xi_{\alpha\beta}$ is 1. The mean free path of dislocations is finally calculated as

$$\frac{1}{\lambda^{\alpha}} = \frac{1}{d_{\text{grain}}} + \sum_{\beta=1}^{N_{\text{twin}}} \xi_{\alpha\beta} \frac{1}{d_{\text{twin}}^{\beta}} \qquad (12)$$

3.2. Model set-up and simulation runs

Based on the constitutive laws outlined above, the CPFE simulations of the steels with their specific grain sizes and phase compositions (as listed in Table 1) under tensile loading were carried out using the finite element solver MSC.Marc2013 in conjunction with the open source user defined material subroutine coded in the DAMASK package [42,45]. The FE mesh includes 8000 eight-noded, isoparametric, three-dimensional brick elements. For the steels consisting of two phases, the elements that are given specific mechanical properties of austenite and martensite are mixed homogeneously. By assigning one grain orientation to the eight integration points pertaining to each finite element, the total number of the initial orientations representing the random starting texture of the steel, as observed after the heat treatment, amounts to 64,000 (8000 × 8). For modeling uniaxial tensile testing, periodic boundary conditions are adopted and a strain rate of 10^{-3} s^{-1} is imposed [46]. The constitutive parameters characterizing the austenite are determined by fitting the macroscopic stress vs. strain curve as well as the twin volume fraction vs. strain curves obtained from the tensile test on the reference sample with an average initial grain size of 35 μm. It should be mentioned that as the slip resistance is related to the strength in a solid solution, the critical resolved shear stress for activating dislocation slip varies among the steels with different grain sizes. Then, based on the Hall–Petch law that is attributed to dislocation pile-ups against grain boundaries, for the austenitic phase the τ_{solute} values of 0.03, 0.37 and 0.65 GPa are used for steels with a grain size of 35 μm, 800 nm and 270 nm, respectively. For the UFG steels, as the austenitic and the martensitic grains collectively contribute to the overall yield strength, the initial slip resistance of the martensite is determined by fitting the corresponding macroscopic stress vs. strain curves. The τ_{solute} values of 1.59 and 2.50 GPa are used for the martensite in steels with a grain size of 800 nm and 270 nm, respectively. For both phases, all other constitutive parameters are identical for the differently grain-sized steels, as listed in Table 2.

3.3. Simulation results

Fig. 4(a) shows the measured and the predicted true stress–strain curves for the steels with different grain sizes, respectively. One could note that some discrepancies exist between experiments and predictions for the studied steels. For the steel with a grain size of 35 μm, as the current simulation does not incorporate the martensitic phase transformation at large strains, at a true strain above ∼0.38 the predicted strength is lower than that obtained by the measurements. For the UFG steels, the overestima-

Table 2
Constitutive material parameters of the austenitic phase and the martensitic phase used for the crystal plasticity simulations. C_{11}, C_{12} and C_{44} are the single crystal elastic constants. Regarding the thermal activated annihilation of dislocations, the following parameters are used: $\rho_{sgl,0}$ and $\rho_{dip,0}$ are the initial dislocation density and dipole density, respectively; v_0 is the initial glide velocity; D_0 is the bulk diffusion coefficient; and Q_{SD} is the activation energy for dislocation climb. The asterisk (*) indicates fitting parameters.

Phase	C_{11}	C_{12}	C_{44}	$\rho_{sgl,0}$	$\rho_{dip,0}$	b
Austenite	204.6 GPa	137.7 GPa	126.2 GPa	1.0×10^{12} m^{-2}	1.0 m^{-2}	2.58×10^{-10} m
Martensite	237.0 GPa	141.0 GPa	116.0 GPa	1.0×10^{12} m^{-2}	1.0 m^{-2}	2.58×10^{-10} m
	v_0	D_0	Q_{SD}^*	Q_0^*	p^*	q^*
Austenite	1.0×10^{-4} m s^{-1}	4.0×10^{-5} m^2 s^{-1}	3.4×10^{-19} J	1.5×10^{-19} J	1.0	1.0
Martensite	1.0×10^{-4} m s^{-1}	20.0×10^{-5} m^2 s^{-1}	3.4×10^{-19} J	1.5×10^{-19} J	1.0	2.55
	b_{twin}	γ_{sf}	s	L_0^*	$\dot{N}_0^*$	r^*
Austenite	1.45×10^{-10} m	0.021 J m^{-2}	0.1 μm	$560 \times b$	2.0×10^{15} s^{-1}	3.0
Martensite	–	–	–	–	–	2.0

tion of both the strength after yielding and the maximum elongation is attributed to the fact that the microstructure of the short-time-annealed steels (150 s for the 270 nm grained steel, 180 s for the 800 nm grained steel) may not be homogeneous. Some dark grains indicate the accumulation of defects whereas the other grains appear less distorted indicating a low defect content (Fig. 2). Therefore, during the tensile tests conducted on the UFG materials the deformation may be inhomogeneous, deteriorating ductility.

Fig. 4(b) shows the strain-hardening responses (strain-hardening rates $d\sigma/d\varepsilon$) of the steels. For the steel with a grain size of 35 μm, below ∼0.1 true strain the decrease of both, the measured and simulated strain-hardening rates indicates that dislocation slip is the main deformation mechanism. At a strain level above ∼0.1, the increasing strain-hardening related to mechanical twinning is clearly identified, which is typical of metals and alloys with low stacking fault energy (SFE) such as silver [47], Cu–Zn alloys [48,49] and TWIP steels [50–52] where twin interfaces play a large role in the hardening of the materials. After ∼0.33 true strain the experiment shows that the strain-hardening rate continues to increase with deformation, whereas the simulation show a significant drop which corresponds to the saturation of the twin volume fraction. Therefore, the deformation stage (∼0.33 true strain) corresponding to the deviation of the modeling from the experiments is attributed to the deformation-induced onset of the martensitic phase transformation.

The simulated twin volume fraction for the same steel as a function of the true strain is presented in Fig. 5(a), showing that approximately 16 vol.% and 27 vol.% of the steel is twinned at true strains of 0.22 and 0.36, respectively. This agrees well with the previously published experimental observations on the same CG steel [36]. For the steels with a grain size of either 800 nm or 270 nm, the strain hardening dominated by twinning is not predicted by the modeling, even though experiments show that the strain-hardening rates of the steels decrease mildly at a true strain above ∼0.03 (Fig. 4(b)). To see this more clearly, the shear contributions of the competing deformation systems (dislocation slip and twinning) obtained from the different simulations are plotted as a function of the true strain in Fig. 5(b). The individual contributions are given as summations over the absolute values of the shear rates on the different systems for each type of mechanism, normalized by the overall shear in each time step. The simulation for the 35 μm grain-sized steel shows that an increase in the twinning shear rate occurs at the initial stage of deformation, and the maximum occurs at a strain of 0.25. With further deformation, the shear rate carried by dislocations increases, indicating that the material is deformed both by slip and by twinning. The difference in strain-hardening response between the experiment and the prediction at this deformation stage is attributed to the absence the martensite transformation in the model. For the 800 nm and
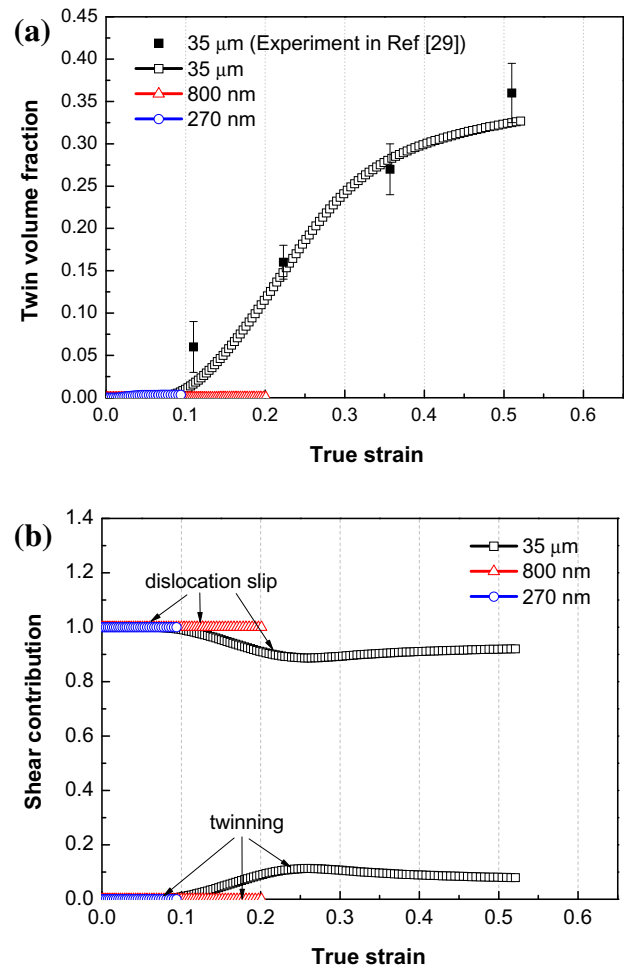

Fig. 5. Predicted (a) twin volume fraction and (b) relative shear contributed by the dislocation slip and twinning systems for the CG and UFG steels as a function of true strain along the tensile axis.

270 nm grain-sized steels, the shear rate on the twin systems that remains on a constant low level during the whole period of plastic straining is predicted. This explains the very minor strain hardening as well as the negligible twin volume fraction as revealed by measurements. Moreover, the experimental results show that only very limited martensite transformation occurs in these steels during tensile testing, which leads to a better prediction of the stress–strain behavior for the UFG steels compared to the CG material.

4. Discussion

4.1. Origin of the ultrahigh strength—Hall–Petch effect

The ultrahigh strength in these UFG 304L SS samples originates mainly from the strengthening due to the Hall–Petch effect [53]:

$$\sigma_y = \sigma_0 + k d^{-1/2} \tag{13}$$

here σ_0 is the friction stress, k is a constant, referred to as grain boundary resistance, and d is the mean grain size. According to Mayers et al. [54], σ_0 is 167 MPa, and $k = 19.05$ MN mm$^{1/2}$ for a 304 SS. Hence, the tensile yield strength as a function of $d^{-1/2}$ for the austenitic phase of the investigated UFG samples can be extrapolated from the Hall–Petch line using the literature data for 304 SS [54] to a mean grain size of 800 nm, yielding a strength of about 840 MPa. This value is lower than but close to the measured yield strength of 1170 MPa for the sample cold-rolled to 67% and annealed at 650 °C. For the sample with an average grain size of 270 nm, the estimated yield strength of the austenite is 1325 MPa, which is also lower than the measured value of 1890 MPa but still captures the strengthening effect with the refinement of grains. Therefore, the Hall–Petch law provides a reasonable prediction of the yield strength for the UFG steels. The discrepancy between the so predicted strength and the measurement is attributed to the pre-existence of martensite in those steels prior to loading.

4.2. Origin of the ultrahigh strength—mechanical twinning effect

To explore the fundamental mechanisms leading to the ultrahigh strength of the UFG austenitic stainless steel, systematic TEM observations have been conducted on the CG and UFG steels after tensile deformation. Fig. 6 shows sections close to the fracture surfaces. For the steels with average grain sizes of 35 μm and 800 nm, a large density of deformation twins with lamella thicknesses of 5–30 nm is identified (Figs. 6(a)–(d)). These twins penetrate the entire grains, whereas some of them have no clearly defined boundaries with one end ending within the grains. Moreover, dense dislocation arrangements accumulate at the twin boundaries as well as at the high-angle grain boundaries. For the steel with an average grain size of 270 nm, we find that multiple dislocations are blocked by grain boundaries, while some micro-twins are also seen in grain interiors (Fig. 6(e)). To study this more closely, high resolution observations are made on the areas indicated by the rectangles, as shown in Figs. 6(f) and (g), respectively. We find that the lamella thicknesses of the twins are below 10 nm. One partial dislocation is emitted from a twin boundary and stopped at the other twin boundary, leaving a stacking fault behind (Fig. 6(f)). In Fig. 6(g), many stacking faults are identified, though some of them are recognized as ε-martensite plates [55]. This nanostructure is very different from the one observed in the CG steels [36], in which most of the plastic deformation occurs in the form of dislocation slip, twinning, and martensitic phase transformation. The statistical analysis of the TEM observations on several areas for each of the deformed steel samples incorporating more than 200 individual grains reveals that the twinned area fraction for the 270 nm, 800 nm and 35 μm grain-sized samples is 3%, 8%, and 36%, respectively. According to the finite element simulation results, twinning is mostly activated in the steel with an average grain size of 35 μm but suppressed in steels with grain sizes of 800 nm and 270 nm, due to the reduced distance between the obstacles acting against twin growth with decreasing grain size. This picture generally agrees with the above-mentioned TEM observations.
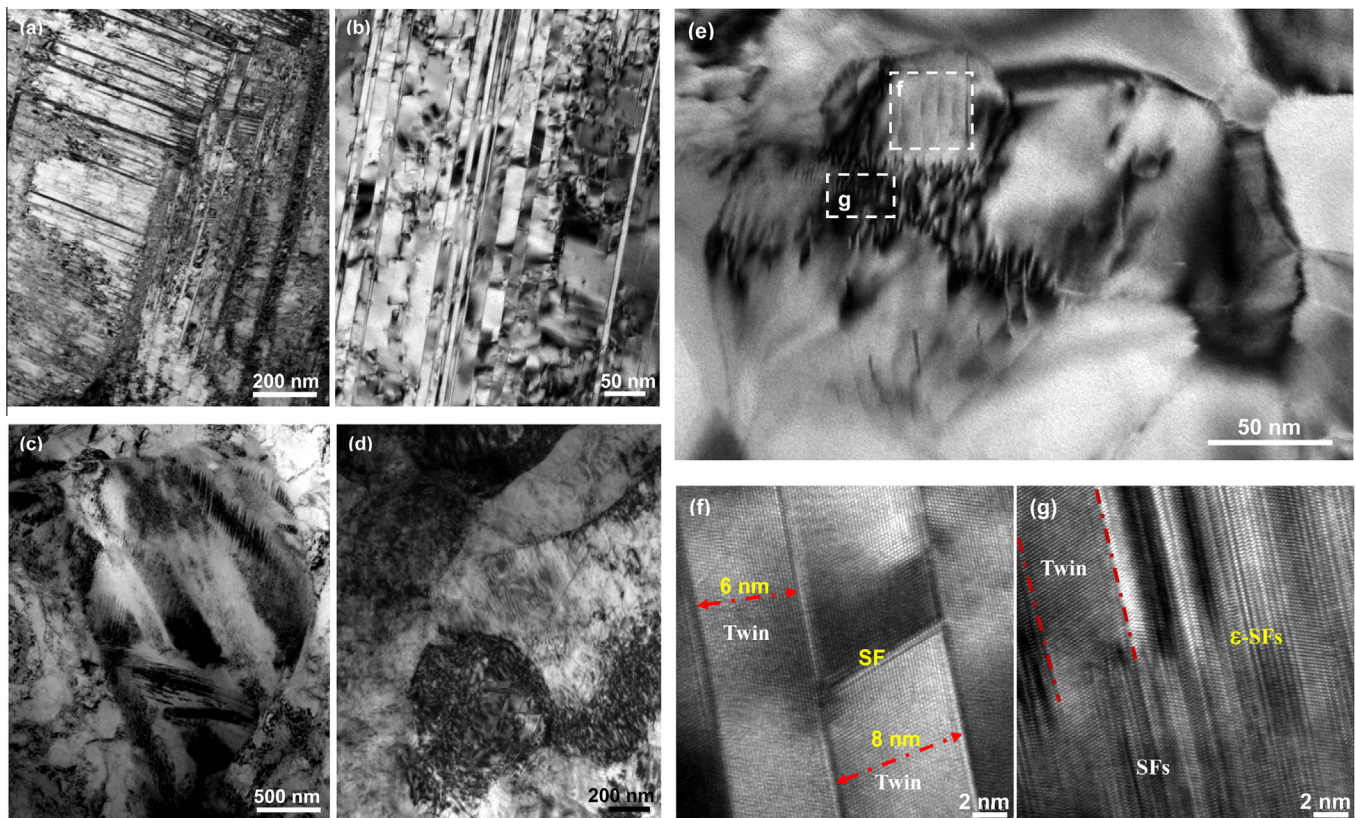

Fig. 6. TEM micrographs showing morphologies of the deformed CG and UFG steels with the average grain size of (a),(b) 35 μm; (c),(d) 800 nm and (e)–(g) 270 nm. (f) and (g) are close observations of the areas indicated by the rectangles in (e). SF: stacking fault.

Recently, Misra et al. [56,57] investigated the deformation behavior of a nano-grained/ultrafine-grained austenitic stainless steel with high strength and high ductility. Their results demonstrated that mechanical twinning was an active deformation mechanism in the steel, while in a CG steel the nucleation of strain-induced martensite occurred at the shear bands. In order to elucidate the transition from dislocation slip to twinning in a NG aluminium, Chen et al. [58] proposed a simple model based on the shear stresses required to initiate a full dislocation and a Shockley partial emitted from grain boundaries, in which the relationship between shear stresses for a full dislocation activation (τ_f) and the grain size (d) is expressed as:

$$\tau_f = \frac{2\alpha Gb}{d} \tag{14}$$

In the case of the localized stress concentration, partial dislocation glide on successive planes can form a large dislocation pile-up at the twin front. Thus, stress multiplication at the first dislocation by pile-up (i.e. $n \cdot \tau$, where n is the number of partial dislocations in the pile-up and τ is the applied shear stress) is an effective way to penetrate or remove obstacles in front of the twin tip [59]. Consequently, the shear stress required to initiate a Shockley partial (τ_p) is:

$$n \cdot \tau_p = \frac{2\alpha Gb}{d} + \frac{\gamma}{b_p} \tag{15}$$

Here α is a parameter with a value of 0.5 for edge dislocations and 1.5 for screw dislocations. It contains the scaling factor between the length of the dislocation source and the grain size [60]. G is the shear modulus, d is the grain size, γ is the stacking fault energy, b and b_p are the Burgers vectors of the full dislocation and of the Shockley partial dislocation, respectively.

Evidently, the number of partial dislocations increases with the decrease of the grain size, since τ_p becomes lower than τ_f when the grain size is reduced to a certain scale due to the enhanced stress concentration under tension. Then it is possible that the deformation mode will switch from slip to slip plus twinning for the material with UFG structures, depending on the emission of partial dislocations from grain boundaries. In this study, because of the low SFE of the austenitic stainless steel, partial dislocations acting as glide dislocation are more widely separated than in high SFE materials. Before a dislocation can leave its primary slip plane and move onto a cross slip plane, the stacking fault between the partials must firstly be compressed, which requires a high stress to overcome the repulsive forces between the partial dislocations. Therefore, cross slip is suppressed and deformation tends to be much more planar in the austenitic steel than in materials with higher SFE. These faults are precursors of deformation twins found in the microstructures. Since the faults and twins are formed progressively with straining, twins in the steels increase gradually via partial dislocation slip. The activated stacking faults and the subsequently formed twin boundaries can effectively refine the microstructure to a scale similar to UFG or NG. The importance of partial dislocations, stacking faults and twins in the plastic deformation of fcc metals has recently been addressed by several authors [22,61,62].

The shear stress for dislocation emission in UFG austenitic steels can be determined with the values in a 304SS: $b = 2.58 \times 10^{-10}$ m, $b_p = 1.45 \times 10^{-10}$ m, $G = 76$ GPa, $\alpha = 1$, and $\gamma = 0.021$ J·m^{-2} [63,64]. Then, the shear stress for partial dislocation emission ($n = 3$, based on the twin nucleation scheme proposed by Mahajan et al. [44]) is 96 MPa, while the emission of a perfect or full dislocation (τ_f) reaches 145 MPa, according to Eqs. (14) and (15). This means that it is easier to activate a partial dislocation than a full dislocation in the ultrafine-grained microstructure with

an average size of 270 nm. However, it is worth noting that in UFG steels the length of partial dislocations required for forming a twin nucleus becomes quite limited compared with the CG samples. Then, the required correlated bow-out of three partial dislocations may not be significant enough to trigger the formation of a twin nucleus, which explains the prevalence of dislocation slip in the 800 nm and 270 nm grained steels as predicted by the simulation.

On the other hand, during plastic deformation the activation of partials is not required due to the pile-up and dissociation of dislocations. Under this condition, Zhu et al. [64] gave an analytical description on nucleation of deformation twins in nanocrystalline fcc metals in terms of critical grain size, d_c':

$$\frac{2.089 - \upsilon}{54.985(1 - \upsilon)} \frac{a^2 G}{\gamma} \leqslant \frac{d_c'}{\ln\left(\sqrt{2}d_c'/a\right)} \leqslant \frac{3.727 + \upsilon}{97.053(1 - \upsilon)} \frac{a^2 G}{\gamma} \tag{16}$$

Here, υ is Poisson's ratio, 0.27, a is the lattice parameter ($a \approx 0.361$ for fcc metals) [65]. The corresponding d_c' for the UFG 304SS is in the range of 210–300 nm. The stress data obtained from Eqs. (14) and (16) appears to be low, when we consider the yield strength of 1890 MPa for the UFG 304SS (i.e. shear stress $\sim$500 MPa, Taylor factor $M = 3.61$). Consequently, it is conceivable that for the ultrafine-grained steel with an average grain size of 270 nm plastic deformation takes place prior to the onset of twinning.

Actually, both the twinning process and the formed deformation twins can improve the work-hardening ability of UFG materials. First, a stacking fault, precursor of twinning, renders cross-slip more difficult because the stacking fault has to be constricted before the dislocation can cross slip. Therefore, gliding dislocations are confined to a thin slip band that forms a large pile-up against an obstacle, forming the region that is analogous to a grain boundary [9]. Large pile-ups can also generate a large long range back stress and result in a high strain-hardening rate. Second, it was well established that strengthening associated with twin boundaries is similar to that caused by less coherent grain boundaries [66]. Molecular dynamics simulations have also demonstrated that once nanoscale twins are formed they can repel certain types of gliding dislocations and give rise to pile-ups, leading to the strain hardening of materials [67].

4.3. Origin of the ultrahigh strength—martensitic transformation effect

The high work-hardening rate observed for the austenitic steels is also associated with the deformation-induced martensitic transformation in these materials [35,64]. As documented in Table 1, for the 800 nm grain-sized sample, after tensile deformation to 12% strain the volume fraction of martensite shows a significant increase from 23% to 38%. For the 270 nm grain-sized sample at 6% strain, the volume increment of martensite is only $\sim$2%. However, for the 35 μm grain-sized steel, a large amount of martensite ($\sim$53 vol.%) induced by 59% tensile deformation is formed and this leads to the significant hardening of the material. Our experimental results hence show that the sample with a grain size of 270 nm is surprisingly stable against the transformation from austenite to martensite, thus the strain-hardening contributed by phase transformation is negligible during the tensile testing. Assuming that the austenite transforms to the martensite via a single variant mode, the increase in the elastic-strain energy can be estimated according to [57,68]:

$$\Delta E_\upsilon = 0.5E_1\varepsilon_1^2(L/d)^2 + (0.5E_2\varepsilon_2^2 + 0.5E_3\varepsilon_3^2)(L/d) \tag{17}$$

where E and ε are the Young's modulus and elastic strain in each lattice plane, respectively. L is the thickness of martensite lath and d is the grain size of austenite. This means that the value of

ΔE_v increases with decreasing grain size of the initial austenite. Consequently, the nucleation ability of the martensite is reduced with the refinement of grains, and the lattice displacement must be accommodated by dislocation slip and twinning in the UFG steels.

5. Conclusions

(1) An UFG austenitic stainless steel with an average grain size of 270 nm has been synthesized by accumulative rolling and annealing. The material shows a yield strength of 1890 MPa, an ultimate-tensile stress of 2050 MPa, and an elongation of 6 ± 1%. The high strength originates mainly from the strengthening effect associated with grain boundaries, according to the Hall–Petch effect.

(2) For the austenitic steels with different grain sizes, when subjected to a uniaxial tensile load, the twinned volume fraction amounts to 3% for the 270 nm grain-sized steel after 6% elongation, 8% for the 800 nm grain-sized steel after 12% elongation, and 36% for the 35 μm grain-sized steel after 59% elongation, respectively. The volume fraction of the martensite is 34%, 38% and 53% for the 270 nm, 800 nm and 35 μm grain-sized steels, respectively. By TEM analysis we find that both, deformation twinning and martensitic phase transformation have been significantly suppressed with the refinement of the initial austenitic grain size.

(3) A crystal plasticity finite element model incorporating the grain size-controlled activation of dislocation slip and deformation twinning captures some of the micromechanical trends observed for the steels with different grain sizes. In combination with the theoretical analysis, we suggest that deformation of instable austenitic UFG steels is dominated by the slip of partial dislocations, whereas for CG steels dislocation slip, twinning and martensitic phase transformation jointly contribute to the plastic straining.

Acknowledgements

References

[1] R.Z. Valiev, Nanostructuring of metals by severe plastic deformation for advanced properties, Nature Mater. 3 (2004) 511–516.

[2] X.H. Chen, J. Lu, L. Lu, K. Lu, Tensile properties of a nanocrystalline 316L austenitic stainless steel, Scr. Mater. 52 (2005) 1039–1044.

[3] Y. Iwahashi, J. Wang, Z. Horita, M. Nemoto, T.G. Langdon, Principle of equal-channel angular pressing for the processing of ultra-fine grained materials, Scr. Mater. 35 (1996) 143–146.

[4] Y. Ivanisenko, R.K. Wunderlich, R.Z. Valiev, H.J. Fecht, Annealing behaviour of nanostructured carbon steel produced by severe plastic deformation, Scr. Mater. 49 (2003) 947–952.

[5] Y. Saito, H. Utsunomiya, N. Tsuji, T. Sakai, Novel ultra-high straining process for bulk materials-development of the accumulative roll-bonding (ARB) process, Acta Mater. 47 (1999) 579–583.

[6] R. Song, D. Ponge, D. Raabe, J.G. Speer, D.K. Matlock, Overview of processing, microstructure and mechanical properties of ultrafine grained bcc steels, Mater. Sci. Eng., A 441 (2006) 1–17.

[7] R. Song, D. Ponge, D. Raabe, Mechanical properties of an ultrafine grained C–Mn steel processed by warm deformation and annealing, Acta Mater. 53 (2005) 4881–4892.

[8] R. Song, D. Ponge, D. Raabe, R. Kaspar, Microstructure and crystallographic texture of an ultrafine grained C–Mn steel and their evolution during warm deformation and annealing, Acta Mater. 53 (2005) 845–858.

[9] M. Calcagnotto, Y. Adachi, D. Ponge, D. Raabe, Deformation and fracture mechanisms in fine- and ultrafine-grained ferrite/martensite dual-phase steels and the effect of aging, Acta Mater. 59 (2011) 658–670.

[10] M. Calcagnotto, D. Ponge, D. Raabe, Effect of grain refinement to 1 mu m on strength and toughness of dual-phase steels, Mater. Sci. Eng., A 527 (2010) 7832–7840.

[11] M. Calcagnotto, D. Ponge, D. Raabe, Microstructure control during fabrication of ultrafine grained dual-phase steel: characterization and effect of intercritical annealing parameters, ISIJ Inter. 52 (2012) 874–883.

[12] S. Cheng, J.A. Spenser, W.W. Milligan, Strength and tension/compression asymmetry in nanostructured and ultrafine-grain metals, Acta Mater. 51 (2003) 4505–4518.

[13] Y.H. Zhao, J.F. Bingert, X.Z. Liao, B.Z. Cui, K. Han, A.V. Serhueeva, A.K. Muhkerjee, R.Z. Valiev, T.G. Langdon, Y.T. Zhu, Simultaneously increasing the ductility and strength of ultra-fine-grained pure copper, Adv. Mater. 18 (2006) 2949–2953.

[14] Y.H. Zhao, X.Z. Liao, S. Cheng, E. Ma, Y.T. Zhu, Simultaneously increasing the ductility and strength of nanostructured alloys, Adv. Mater. 18 (2006) 2280–2283.

[15] Y.F. Shen, L. Lu, Q.H. Lu, Z.H. Jin, K. Lu, Tensile properties of copper with nano-scale twins, Scr. Mater. 52 (2005) 989–994.

[16] L. Lu, Y.F. Shen, X.H. Chen, L.H. Qian, K. Lu, Ultrahigh strength and high electrical conductivity in copper, Science 304 (2004) 422–426.

[17] L. Lu, X.H. Chen, X.X. Huang, K. Lu, Revealing the maximum strength in nanotwinned copper, Science 323 (2009) 607–610.

[18] V. Shrinivas, S.K. Varma, L.E. Murr, Deformation-induced martensitic characteristics in 304-stainless and 316-stainless steels during room-temperature rolling, Metall. Mater. Trans. A 26 (1995) 661–671.

[19] E. Cakmak, H. Choo, K. An, Y. Ren, A synchrotron X-ray diffraction study on the phase transformation kinetics and texture evolution of a TRIP steel subjected to torsional loading, Acta Mater. 60 (2012) 6703–6713.

[20] K.X. Tao, D.W. Brown, S.C. Vogel, H. Choo, Texture evolution during strain-induced martensite phase transformation in 304L stainless steel at a cryogenic temperature, Metall. Mater. Trans. A 37 (2006) 3469–3475.

[21] N. Li, Y.D. Wang, W.J. Liu, Z.N. An, J.P. Liu, R. Su, J. Li, P.K. Liaw, In situ X-ray microdiffraction study of deformation-induced phase transformation in 304 austenitic stainless steel, Acta Mater. 64 (2014) 12–23.

[22] S. Rajasekhara, P.J. Ferreira, Martensite→austenite phase transformation kinetics in an ultrafine-grained metastable austenitic stainless steel, Acta Mater. 59 (2011) 738–748.

[23] X. Peng, J. Yan, Y. Zhou, F. Wang, Effect of grain refinement on the resistance of 304 stainless steel to breakaway oxidation in wet air, Acta Mater. 53 (2005) 5079–5088.

[24] J.-H. Kim, B.K. Kim, D.-I. Kim, P.-P. Choi, D. Raabe, K.-W. Yi, The role of grain boundaries in the initial oxidation behavior of austenitic stainless steel containing alloyed Cu at 700 °C for advanced thermal power plant applications, Corros. Sci. 96 (2015) 52–66.

[25] B.R. Kumar, D. Raabe, Tensile deformation characteristics of bulk ultrafine-grained austenitic stainless steel produced by thermal cycling, Scr. Mater. 66 (2012) 634–637.

[26] Z. Yanushkevich, A. Belyakov, R. Kaibyshev, Microstructural evolution of a 304-type austenitic stainless steel during rolling at temperatures of 773–1273 K, Acta Mater. 82 (2015) 244–254.

[27] T. Sakai, A. Belyakov, R. Kaibyshev, H. Miura, J.J. Jonas, Dynamic and post-dynamic recrystallization under hot, cold and severe plastic deformation conditions, Prog. Mater Sci. 60 (2014) 130–207.

[28] Y. Estrin, A. Vinogradov, Extreme grain refinement by severe plastic deformation: a wealth of challenging science, Acta Mater. 61 (2013) 782–817.

[29] N. Dudova, A. Belyakov, T. Sakai, R. Kaibyshev, Dynamic recrystallization mechanisms operating in a Ni–20%Cr alloy under hot-to-warm working, Acta Mater. 58 (2010) 3624–3632.

[30] Y. Huang, J.D. Robson, P.B. Prangnell, The formation of nanograin structures and accelerated room-temperature theta precipitation in a severely deformed Al-4 wt.% Cu alloy, Acta Mater. 58 (2010) 1643–1657.

[31] D.A. Hughes, N. Hansen, High angle boundaries formed by grain subdivision mechanisms, Acta Mater. 45 (1997) 3871–3886.

[32] W.S. Lee, C.F. Lin, Comparative study of the impact response and microstructure of 304L stainless steel with and without prestrain, Metall. Mater. Trans. A 33 (2002) 2801–2810.

[33] W.S. Lee, C.F. Lin, T.H. Chen, M.C. Yang, High temperature microstructural evolution of 304L stainless steel as function of pre-strain and strain rate, Mater. Sci. Eng., A 527 (2010) 3127–3137.

[34] T. Suzuki, H. Kojima, K. Suzuki, T. Hashimoto, M. Ichihara, An experimental study of the martensite nucleation and growth in 18/8 stainless steel, Acta Metall. 25 (1977) 1151–1162.

[35] G.B. Olson, M. Cohen, Kinetics of strain-induced martensitic nucleation, Metall. Trans. A 6 (1975) 791–795.

[36] Y.F. Shen, X.X. Li, X. Sun, Y.D. Wang, L. Zuo, Twinning and martensite in a 304 austenitic stainless steel, Mater. Sci. Eng., A 552 (2012) 514–522.

[37] D. Raabe, Texture and microstructure evolution during cold rolling of a strip cast and of a hot rolled austenitic stainless steel, Acta Mater. 45 (1997) 1137–1151.

[38] C. Herrera, D. Ponge, D. Raabe, Design of a novel Mn-based 1 GPa duplex stainless TRIP steel with 60% ductility by a reduction of austenite stability, Acta Mater. 59 (2011) 4653–4664.

[39] W.Y. Xue, Y.F. Shen, D.F. Liu, Z.Y. Liu, Y.D. Wang, Strength and ductility of ultrafine grained 304ss prepared by accumulative rolling and annealing, in: Characterization of Minerals, Metals, and Materials, TMS (The Minerals, Metals & Materials Society), 2013, pp. 45–52.

[40] S.R. Kalidindi, Modeling anisotropic strain hardening and deformation textures in low stacking fault energy fcc metals, Int. J. Plast. 17 (2001) 837–860.

[41] W. Blum, P. Eisenlohr, Dislocation mechanics of creep, Mater. Sci. Eng., A 510–511 (2009) 7–13.

[42] F. Roters, P. Eisenlohr, L. Hantcherli, D.D. Tjahjanto, T.R. Bieler, D. Raabe, Overview of constitutive laws, kinematics, homogenization and multiscale methods in crystal plasticity finite-element modeling: Theory, experiments, applications, Acta Mater. 58 (2010) 1152–1211.

[43] L. Kubin, B. Devincre, T. Hoc, Modeling dislocation storage rates and mean free paths in face-centered cubic crystals, Acta Mater. 56 (2008) 6040–6049.

[44] S. Mahajan, G.Y. Chin, Formation of deformation twins in f.c.c. crystals, Acta Metall. 21 (1973) 1353–1363.

[45] F. Roters, P. Eisenlohr, C. Kords, D.D. Tjahjanto, M. Diehl, D. Raabe, DAMASK: the Düsseldorf advanced material simulation kit for studying crystal plasticity using an FE based or a spectral numerical solver, Proc. IUTAM 3 (2012) 3–10.

[46] Z. Zhao, M. Ramesh, D. Raabe, A.M. Cuitino, R. Radovitzky, Investigation of three-dimensional aspects of grain-scale plastic surface deformation of an aluminum oligocrystal, Int. J. Plast. 24 (2008) 2278–2297.

[47] H. Paul, J.H. Driver, C. Maurice, A. Piątkowski, The role of shear banding on deformation texture in low stacking fault energy metals as characterized on model Ag crystals, Acta Mater. 55 (2007) 575–588.

[48] T. Leffers, R.K. Ray, The brass-type texture and its deviation from the copper-type texture, Prog. Mater. Sci. 54 (2009) 351–396.

[49] N. Jia, F. Roters, P. Eisenlohr, C. Kords, D. Raabe, Non-crystallographic shear banding in crystal plasticity FEM simulations: example of texture evolution in α-brass, Acta Mater. 60 (2012) 1099–1115.

[50] D.R. Steinmetz, T. Jäpel, B. Wietbrock, P. Eisenlohr, I. Gutierrez-Urrutia, A. Saeed-Akbari, T. Hickel, F. Roters, D. Raabe, Revealing the strain-hardening behavior of twinning-induced plasticity steels: Theory, simulations, experiments, Acta Mater. 61 (2013) 494–510.

[51] O. Bouaziz, S. Allain, C. Scott, Effect of grain and twin boundaries on the hardening mechanisms of twinning-induced plasticity steels, Scr. Mater. 58 (2008) 484–487.

[52] I. Gutierrez-Urrutia, D. Raabe, Dislocation and twin substructure evolution during strain hardening of an Fe-22 wt.% Mn–0.6 wt.% C TWIP steel observed by electron channeling contrast imaging, Acta Mater. 59 (2011) 6449–6462.

[53] N.J. Petch, The cleavage strength of polycrystals, J. Iron. Steel. Inst. 174 (1953) 25–28.

[54] M.A. Mayers, K.K. Chawla, Mechanical Behavior of Materials, Prentice Hall, Inc., Upper Saddle River, New Jersey, 1999. 07458, pp. 271–272.

[55] Y.F. Shen, Y.D. Wang, X.P. Liu, X. Sun, R. Lin Peng, S.Y. Zhang, L. Zuo, P.K. Liaw, Deformation mechanisms of a 20 Mn TWIP steel investigated by in situ neutron diffraction and TEM, Acta Mater. 61 (2013) 6093–6106.

[56] R.D.K. Misra, Z. Zhang, Z. Jia, L.P. Karjalainen, Probing deformation processes in near-defect free volume in high strength high ductility nanograined/ultrafine-grained (NG/UFG) metastable austenitic stainless steels, Scr. Mater. 63 (2010) 1057–1060.

[57] R.D.K. Misra, V.S.A. Challa, Y.F. Shen, M.C. Somani, L.P. Karjalainen, Interplay between grain structure, deformation mechanisms and austenite stability in phase-reversion-induced nanograined/ultrafine-grained austenitic ferrous alloy, Acta Mater. 84 (2015) 339–348.

[58] M.W. Chen, E. Ma, K.J. Hemker, Y.M. Wang, X. Cheng, Deformation twinning in nanocrystalline aluminium, Science 300 (2003) 1275–1277.

[59] Y.M. Wang, M.W. Chen, F.H. Zhou, E. Ma, High tensile ductility in a nanostructured metal, Nature 419 (2002) 912–915.

[60] Y.T. Zhu, X.L. Wu, X.Z. Liao, J. Narayan, L.J. Kecskes, S.N. Mathaudhu, Dislocation–twin interactions in nanocrystalline fcc metals, Acta Mater. 59 (2011) 812–821.

[61] W.W. Jian, G.M. Cheng, W.Z. Xu, H. Yuan, M.H. Tsai, Q.D. Wang, C.C. Koch, Y.T. Zhu, S.N. Mathaudhu, Ultrastrong Mg alloy via nano-spaced stacking faults, Mater. Res. Lett. 1 (2013) 61–66.

[62] V. Yamakov, D. Wolf, S.R. Phillpot, H. Gleiter, Dislocation–dislocation and dislocation–twin reactions in nanocrystalline Al by molecular dynamics simulation, Acta Mater. 51 (2013) 4135–4147.

[63] L.E. Murr, K.P. Staudhammer, S.S. Hecker, Effects of strain state and strain rate on deformation-induced transformation in 304 stainless steel: part II. Microstructural study, Metall. Trans. A 13 (1982) 627–635.

[64] Y.T. Zhu, X.Z. Liao, S.G. Srinivasan, E.J. Lavernia, Nucleation of deformation twins in nanocrystalline face-centered-cubic metals processed by severe plastic deformation, J. Appl. Phys. 98 (2005) 1–7.

[65] H.W. Zhang, Z.K. Hei, G. Liu, J. Lu, K. Lu, Formation of nanostructured surface layer on AISI 304 stainless steel by means of surface mechanical attrition treatment, Acta Mater. 51 (2003) 1871–1881.

[66] W.J. Babyak, F.N. Rhines, The relationship between the boundary area and hardness of recrystallized cartridge brass, Trans. Mettall. Soc. AIME 218 (1960) 21–23.

[67] D. Wolf, V. Yamakov, S.R. Phillpot, A. Mukherjee, H. Gleiter, Deformation of nanocrystalline materials by molecular-dynamics simulation: relationship to experiments?, Acta Mater 53 (2005) 1–40.

[68] S. Takaki, K. Fukunaga, J. Syarif, T. Tsuchiyama, Effect of grain refinement on thermal stability of metastable austenitic steel, Mater. Trans. 45 (2004) 2245–2251.